Performance Analysis of a Scalable Navigation Solution using Vehicle Safety Sensors

S. Martin, C. Rose, J. Britt, D. Bevly
College of Engineering
Auburn University
Auburn, AL USA

Zeljko Popovic
Automobile Technology Research
Honda R&D Americas, Inc.
Southfield, MI USA
zpopovic@oh.hra.com

Abstract — **GPS receiver performance can suffer in difficult environments such as urban canyons and heavy foliage. Inertial sensors provide information between GPS updates and can enhance the position solution in a GPS/INS architecture. Additional information from safety sensors already on the vehicle, such as lane departure warning (LDW) sensors, can enhance the navigation solution further by constraining inertial errors even in the presence of GPS errors. This paper outlines a scalable navigation solution that can use a combination of GPS, reduced inertial sensors, full inertial data, vehicle CAN data, and vision sensors, depending on what data is available in difficult environments. Data was collected in Detroit, Michigan in a diverse mix of environments that includes heavy foliage, highway, and downtown areas, in proportions representative of what is expected in typical driving. Validation of the approach consists of both a qualitative analysis of the resulting trajectories overlaid on a map of the area and quantitative comparison of the trajectories produced by the proposed system and the reference system.**

Keywords- positioning; localization; sensor fusion; urban canyon; foliage; GPS; INS; IMU; inertial; navigation; vision; camera; lidar.

I. INTRODUCTION

Intelligent vehicles of the future demand precise and robust localization for improved safety and performance. This information is typically provided by systems that integrate GPS with inertial navigation (INS). The features and quality of these systems vary and their performance differs across various environments. GPS is especially dependent on the line of sight to satellites, and presence of obstructions such as buildings or foliage can reduce the accuracy of GPS. New mass-produced passenger vehicles are starting to use additional sensors for safety systems, such as cameras and lidars (light detection and ranging). With these new sensors come new capabilities that can be leveraged in advanced positioning solutions to combat the errors in GPS that arise due to obstructed views of the sky.

The integrated GPS/INS navigation system is a well-established localization architecture [1][2]. GPS updates provide a means for bounding error growth in the INS solution, while the INS solution bridges GPS gaps. Recently, reduced inertial sensor systems (RISS) have been combined with vehicle speed to provide pose estimates with limited acceleration and angular rate information [3][4]. Moving forward, these systems will be augmented with information from vision based systems to aid GPS in error mitigation.

Lidars and camera systems are used in detection of, or ranging to, distinct features in the environment. For vehicle positioning, these sensors often rely on tracking the change in vehicle position with respect to nearby buildings or lane markings. Lidar-based lane-marking detection has been performed using histogram and histogram gradient feature extraction algorithms in [5][6]. Additionally, work by [7] compared results of lane marking detection by lidar and camera, including estimation of vehicle position in the lane. Lane departure warning (LDW) systems using cameras are currently available. A system is developed in [8] using a linear-parabolic lane model. Hough transform methods were used to obtain road edges in [9], and clothoid model parameters used for horizontal and vertical road parameter recognition in [10].

Integration of global navigation solutions, such as those from GPS/INS systems, with local information from camera or lidar, often requires additional knowledge of the environment in the form of maps. Map matching is of particular importance in [11]. Miller and Campbell enhanced accuracy and robustness of a GPS/INS system by fusing it with vision-based measurements in a particle filter [12]. Another particle filtering application, [13], was able to show centimeter level accuracy in simulation when fusing mono-camera, low cost GPS, and map data.

The variety of sensors available on current and future production vehicles, and the variety of approaches to integrate them, present a unique opportunity for a scalable navigation solution. The term "scalable" highlights the fact that the proposed system integrates a number of possible inputs (depending on the available sensor information) to provide estimates of the vehicle pose. The accuracy and reliability of such a system depends on the available sensor suite. The presented work will show the performance of navigation algorithms using information ranging from as little as two accelerometers and one gyroscope combined with L1-frequency-only GPS, to a full six degree of freedom inertial measurement unit (IMU) with L1 and L2 frequency GPS accompanied by lateral positions from lidar and camera. A map database of the lane markings will be used for vision-based measurement integration. Vehicle wheel speeds from the in-vehicle CAN network will also be incorporated. Validation of the results will consist of both qualitative analysis, by inspection of trajectories plotted on satellite imagery, and quantitative analysis, by differencing between trajectories from proposed algorithms and from the reference system, in order to derive position error statistics.

II. NAVIGATION ALGORITHMS

The navigation algorithm is an extended Kalman filter implementation. Three sensor combinations were examined in this work. The first combined a reduced inertial sensor system, L1 frequency GPS pseudorange and pseudorange rate, and vehicle wheel speed. The second system added L2 frequency GPS measurements. The final system used the six degree of freedom IMU instead of the reduced IMU and also added lateral lane position updates from the camera and lidar. Each implementation is discussed in detail in this section.

A. RISS

Single frequency GPS measurements were integrated with two accelerometers, a single gyroscope, and vehicle speed measurements to form the production grade navigation system for this study. The sensitive axes of the accelerometers were aligned with the longitudinal and lateral axis of the vehicle, and the sensitive axis of gyroscope was aligned with the vertical axis of the vehicle.

The states of the filter are: the position of the vehicle in geodetic coordinates (latitude (λ), longitude (ϕ), and altitude (h), the velocity in a local tangent plane (north (V_n), east (V_e), and down (V_d)), the heading (ψ) of the vehicle relative to north in the local tangent plane, two accelerometer bias states (b_{ax}, b_{ay}), one gyroscope bias state (b_{gz}), GPS receiver clock bias (Δt) and drift ($\dot{\Delta t}$), and a tire slip state (s). Kinematic relationships were used to formulate the dynamic equations for the propagation of the vehicle position states. Note that R_λ and R_φ are the meridian radius and normal radius respectively.

$$\dot{\lambda} = \frac{V_n}{R_\lambda + h} \tag{1}$$

$$\dot{\phi} = \frac{V_e}{\left(R_\phi + h\right)\cos(\lambda)} \tag{2}$$

$$\dot{h} = -V_d \tag{3}$$

The dynamics of the velocities were approximated by the accelerometer measurements (f_{ax}, f_{ay}), the expected measurement error, and the assumption that the vertical velocity was driven by zero mean white noise.

$$\dot{V_n} = (f_{ax} - b_{ax})\cos(\psi) - \left(f_{ay} - b_{ay}\right)\sin(\psi) \tag{4}$$

$$\dot{V_e} = (f_{ax} - b_{ax})\sin(\psi) + \left(f_{ay} - b_{ay}\right)\cos(\psi) \tag{5}$$

$$\dot{V_d} = 0 \tag{6}$$

The heading dynamics were defined relative to the angular velocity measured by the gyroscope ω_{gz}, the measurement error b_{gz}, and the dynamics introduced by the dynamics of the Earth ω_e.

$$\dot{\psi} = \omega_{gz} - b_{gz} - \omega_e \sin(\lambda) \tag{7}$$

IMU biases were assumed to be first order Gauss Markov processes as is the tire slip state. For additional information on these dynamics, see [2][14]. The clock bias dynamics are driven by the drift term and the clock drift is assumed to be driven by zero mean white noise.

The Kalman filter covariance matrix was propagated using the linearized error dynamics derived from the dynamics described above (detailed further in [1]). Note that in this formulation the vehicle roll and pitch were assumed to be negligible as is the lever arm between the IMU and GPS antenna.

The INS navigation solution was updated using both GPS and wheel speed measurements. GPS pseudorange and pseudorange rate measurements were used in this formulation. The INS solution was used to predict the pseudorange and pseudorange rate for each visible satellite at each GPS measurement. The pseudorange prediction model was as follows:

$$\hat{\rho} = \sqrt{(x_s - x)^2 + (y_s - y)^2 + (z_s - z)^2} + c\Delta t \tag{8}$$

where x_s, y_s, and z_s are the Earth centered Earth fixed (ECEF) coordinates of the satellite, and x, y, and z are the estimates of the vehicle position in the ECEF frame. The receiver clock error is labeled $c\Delta t$. The pseudorange rate prediction is given by:

$$\hat{\dot{\rho}} = \frac{(V_{xs} - V_x)(x_s - x) + \left(V_{ys} - V_y\right)(y_s - y) + (V_{zs} - V_z)(z_s - z)}{\sqrt{(x_s - x)^2 + (y_s - y)^2 + (z_s - z)^2}} + c\dot{\Delta t} \tag{9}$$

where V_{xs}, V_{ys}, and V_{zs} are the velocities of the satellite in the ECEF frame, and V_x, V_y, and V_z are the estimated vehicle velocities in the ECEF frame.

The pseudorange and pseudorange rate predictions were compared to the measurements to calculate the navigation solution correction. Using the linearized geometry matrix, derived by computing the partial derivative of the pseudorange and pseudorange rate models with respect to the state vector, the correction was mapped into the state domain and applied to the navigation solution and the error covariance matrix was updated.

An additional state update was performed using the encoder-provided wheel position measurement in terms of pulses per revolution. This measurement was converted to wheel speed using the wheel radius and the number of pulses per revolution. The two rear wheel speeds were then averaged to form one observable. This value was then compared to the wheel speed predicted by the INS solution. The model for the wheel speed prediction contains the estimated north and east velocities and the estimated tire slip.

$$\hat{v}_{ws} = (V_n^2 + V_e^2)^2(1 + s) \tag{10}$$

The correction to the position solution is computed by calculating the difference between the predicted and measured wheel speed and mapping that error into the state domain using the geometry matrix. Note also that the stationary condition (i.e., the measured wheel speed is zero) allows for improved estimates of the inertial biases. This is called a zero velocity update, and is further described in [15].

B. GPS/INS

Unlike with the reduced inertial navigation algorithm, when the full six degree of freedom IMU was used, the total attitude (i.e., roll, pitch, and heading) was estimated. Also, rather than navigating in the local tangent plane (used to minimize complexity of mapping the IMU to the navigation frame), the ECEF frame was selected as the navigation frame (minimizing the complexity of mapping the GPS to the navigation frame).

The change of navigation frames impacts the dynamic equations used in the propagation step of the Kalman filter. A rotation matrix was maintained to map accelerometer measurements from the vehicle body frame to the navigation frame. The dynamics of this rotation matrix, C_b^e were given by:

$$\dot{C}_b^e = C_b^e \Omega_{ib} - \Omega_{ie} C_b^e \tag{11}$$

where Ω_{ib} is the measured angular velocity of the body frame relative to an inertial frame and Ω_{ie} is the rotation rate of the Earth. Note that the gyroscope biases must be removed.

The velocity dynamics are now written in vector form as a function of the three axes accelerometer measurements accounting for the effects of gravity on the measured accelerations.

$$\dot{V^e} = C_b^e \left(f_{a_b} - b_{a_b}\right) + g_e \tag{12}$$

Here, f_{a_b} are the three axes accelerometer measurements, b_{a_b} are the accelerometer biases, and g_e is the local acceleration due to gravity.

Since the velocity and position are now expressed in a common navigation frame, the position dynamic equations are straightforward with P^e equal to the x, y, and z components of the position of the vehicle expressed in the ECEF frame.

$$\dot{P}^e = V^e \tag{13}$$

Processing the GPS pseudorange and pseudorange rate measurements follows the same procedure previously described for the RISS implementation. The measurement models can be found in equations 8 and 9. Note that the NovAtel GPS receiver provided measurements from both the L1 and L2 frequency carrier. This typically results in two times the number of observables at each GPS measurement epoch. The wheel speed measurement update was also performed according to the previous formulation.

C. Full Vision Integration

The full vision integration system uses six degree of freedom inertial measurements, dual frequency NovAtel GPS measurements, two estimates of lateral position within the lane – one provided by the lidar and another by the camera, and a map of the lane to estimate the pose of the vehicle. The estimation procedure followed the form described for the GPS/INS algorithm with the addition of a new update step when lateral position measurement were provided by either vision-based sensor. The lane detection and positioning methods for each vision system are described briefly below. A description of the procedure for integrating the measurements in the Kalman filter follows.

1) Lidar Lane Detection

The lidar-based lane detection algorithm is based on fitting an ideal lane model to actual road data, where the ideal lane model is updated with each lidar scan to reflect the current road conditions. Ideally a lane takes on a profile similar to the 100 averaged lidar reflectivity scans seen in Figure 1, where the corresponding road is seen in the lower image. The plot is a mirror image of the photo due to the fact that the right portion of the image corresponds to negative horizontal angles. Note that this profile has a relatively constant area between the peaks, where the peaks represent the lane markings, which are typically bright and thus have higher reflectivity. The constant area is the unmarked pavement of the road surface, which is typically dark and thus has lower reflectivity. An ideal lane model is generated with each lidar scan to mimic this averaged data, where the constant portion is generated by averaging the reflectivity directly in front of the vehicle and the lane markings are generated by increasing the average road surface reflectivity by 75%. This model is then stretched over a range of some minimum expected lane width to some maximum expected lane width, and the minimum RMSE between the ideal lane and the lidar data is assumed to be the area where the lane resides. For additional information on this method, see [16].

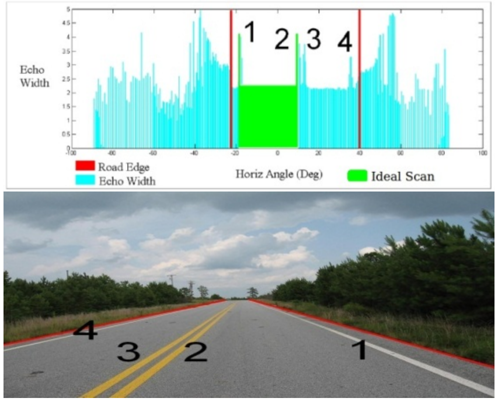

Figure 1: Reflectivity scan from lidar and corresponding road image

2) Camera Lane Detection

The camera-based method uses line extraction techniques applied to the image to detect lane markings and calculate a lateral distance from a 2nd order polynomial model for the lane marking. A threshold is chosen from the histogram of the image to compensate for differences in lighting, weather, or other non-ideal scenarios for extracting the lane markings. The thresholding operation transforms the image into a binary image, which is followed by Canny edge detection. The Hough transform is then used to extract the lines from the image, fill in holes in the lane marking edges, and exclude erroneous edges. Using the slope of the lines, the lines are divided into left or right lane markings. Two criteria are used to further exclude non-lane markings in the image based on the assumption that the lane markings do not move significantly within the image from frame to frame. The first test checks that the slope of the line is within a threshold of the slope of the near region of the last frame's 2nd order polynomial model. The second test uses boundary lines from the last frame's 2nd order polynomial to exclude lines that are not near the current estimate of the polynomial. The 2nd order polynomial interpolation is used on the selected lines' midpoint and endpoints to determine the coefficients of the polynomial model, and a Kalman filter is used to filter the model to decrease the effect of erroneous polynomial coefficient estimates. Finally, the lateral distance is calculated using the polynomial model on the lowest measurable row of the image (for greater resolution) and a real-distance-to-pixel factor. For more information on this method, see [17].

3) Vision Measurement Update

The described camera and lidar algorithms provide *measurements* of the lateral position of the vehicle relative to the center of the lane (Figure 2).

A *prediction* of the lateral position of the vehicle within lane is calculated using the current estimate of the vehicle position and its two closest lane map points in the direction of travel. If the estimated position is inaccurate, incorrect lane coordinates may be selected in the map. This is a limitation of this approach. The distance of the vehicle is calculated normal to the line defined by the two closest points in the north and east directions using the following equations:

$$\mu = \frac{(p_n - m_{2_n})(m_{1_n} - m_{2_n}) + (p_e - m_{1_e})(m_{1_e} - m_{2_e})}{(m_{1_n} - m_{2_n})^2 + (m_{1_e} - m_{2_e})^2} \qquad (14)$$

$$n_n = m_{1_n} + \mu\left(m_{2_n} - m_{1_n}\right) \qquad (15)$$

$$n_e = m_{1_e} + \mu\left(m_{2_e} - m_{1_e}\right) \qquad (16)$$

$$\hat{r} = \sqrt{(p_n - n_n)^2 + (p_e - n_e)^2} \qquad (17)$$

where m_1 and m_2 are the closest map points and $\hat{r}$ is the calculated lateral distance.

The predicted lateral distance, $\hat{r}$, is compared to the camera- or lidar-measured distance, $\tilde{r}$, to calculate correction error. The camera and lidar measurements are applied independently when either algorithm reports a lateral position. The lateral error is then mapped into the state domain using the linearized geometry matrix. Lastly the state estimates and error covariance are updated.

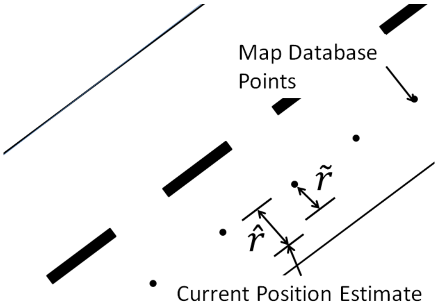

Figure 2: Lateral distance prediction ($\hat{r}$) and measurement ($\tilde{r}$)

III. TEST PROCEDURE

Testing occurred in Detroit, Michigan. Data was captured following a 46-mile route through the city center and surrounding suburbs to mimic driving experienced by a typical driver. In an attempt to capture the full range of GPS satellite geometry variability, the testing occurred over three days. This paper presents results from the first day of testing.

A. *Test Route Selection*

The test route was designed with two main aims: 1) to cover a variety of environment types that have characteristic effects on positioning performance, and 2) to be representative of typical U.S. driving in the proportioning of environment type selections. The environmental features considered important here for their influence on GNSS-based positioning accuracy and for their commonality are trees, tree canopies, mountains, overpasses, buildings, urban canyons, and tunnels. These features, along with other helpful attributes, are used to define seven sufficiently distinct environments in Table 1. This is partially modeled after the table in [18] on page 529. The test route here ensures that the Open and Urban environment types are covered.

Table 1: Environment Definitions

Environment		Features				
		Terrain	**Vegetation**	**Buildings**	**Overpasses**	**Tunnels**
	Open	flat or mildly undulating; mask ⩽ 5°	almost none	almost none	none	none
Rural	**Sparse**		scattered trees	rare, low, far	none	none
	Moderate	mountains masking 5-20°	some tree canopies	some low	maybe but rare	
	Dense	mountains mask 20-60°	dominant tree canopies	negligible compared to natural obstructions although there could be a long tunnel		
Urban	**Sparse**	usually flat or mildly undulating with mask ⩽ 5	scattered trees	some, low or far	none	none
	Moderate		moderate number, some short canopies	multi-story, rare high-rises	some	rare
	Dense			dominant high-rise canyons	frequent	long

FHWA's data on U.S. road use in terms of total miles traveled in each road-class category [19] was used as the best available statistical data to indicate environment proportioning typically encountered in the U.S, even though it does not actually classify roads according to sky-visibility environments, but rather according to road size and volume. The selection of the test route was then guided by the goal of having the roads comprising the route closely match (within ±5%) the urban road-use class proportioning in the found by FHWA. The resulting 46-mile test route is shown in Figure 3.

B. *Test Timing*

Due to satellite geometry variability over time, the test timing is a critical component of the test plan. Since the satellite configuration, as seen by the receiver on the ground, repeats every 24 hours, for repeatable results, it is desirable to have the testing span 24 hours. For procedural convenience, the 24 hour period is divided into 3 shifts. Each shift is on a different day (thus allowing a large break from test driving), and spans 10 hours, with 2-hour overlaps with respect to time of day, for a total desired span of 24 hours.

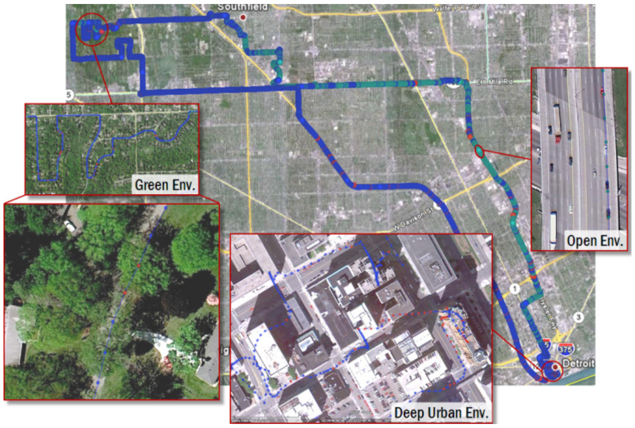

Figure 3: Test Route Overview

C. *Sensors*

Some sensors used here (Table 2) mimic those commonly found on modern-day passenger vehicles. Higher end sensors are also included to acknowledge the expected improvement in sensor capabilities for future production vehicles. Sensors are tested in several combinations.

Table 2: All Sensors Used in Testing

Type	Model	Description	Rate (Hz)
Production or Near-Production Grade			
GPS	NovAtel Propak V3	Scientific GPS receiver, but position, velocity, and L1 data used only	5
Wheel Speed	From in-vehicle CAN network	Production sensor for vehicle wheel speed	50
RISS	Crossbow IMU 440, reduced	Reduced data set used for mimicking near-production grade	100
Camera	Logitech Quickcam 9000	Web-camera, production-like quality	10
Beyond Production Grade			
GPS	NovAtel Propak V3	Scientific GPS receiver gives: position, velocity, L1 and L2 pseudorange and pseudorange rate	5
IMU	Crossbow IMU 440, full	Six degree of freedom IMU, Micro-Electro-Mechanical (MEMS)	100
Lidar	Ibeo Alasca XT	marketed as automotive-grade but not typically available on production vehicles	10
Reference System			
GPS	NovAtel SPAN-SE	Scientific GPS receiver	5
IMU	Honeywell HG1700 AG58	Military-grade IMU	100
External encoder	Peiseler MT1000/r	Mounted on passenger-side rear wheel to count wheel rotations	Speed dependent
DGPS	Differential GPS solution was calculated in post-processing by differencing on-vehicle GPS data with data from local GPS reference stations to mitigate atmospheric effects. Typically, this processing limits global position errors to decimeter level.		

D. Vehicle

The test vehicle was a four door sedan. The NovAtel receiver under test and the NovAtel reference receiver shared the GPS antenna mounted centrally on the roof. Additionally, an external wheel odometer was mounted on the passenger-side rear wheel to aid the reference system. Both the camera and lidar were attached to a roof rack and centered laterally. Data was logged using a full-sized PC in the trunk.

IV. RESULTS

Results are presented in the form of a plot of satellite availability, tables showing error statistics, and plots of navigation solutions on road maps. In Figure 4, the number of visible satellites and the resulting horizontal dilution of precision (HDOP) are shown for the test route over three test runs. As seen, the number of visible satellites varies from twelve to one. Accordingly, the HDOP ranges from typical values (less than 2 [18]) to extreme values when less than four satellites are visible. The GPS positioning accuracy is compromised due to the reduced GPS satellite visibility and increased multipath reflections in portions of the test route. This information is not used directly in the position estimate but provides insight to variations in the achievable accuracy. Note that the HDOP and an approximation for the one sigma user-equivalent range error (UERE) can be used to calculate the expected one sigma horizontal error bound. For a HDOP value of 2 and an UERE of 5.1 meters the expected one sigma horizontal error bound is 10.2 meters [21].

The results of the NovAtel GPS-only solution and the GPS/INS solution combining the NovAtel receiver data with the full six degree of freedom IMU440 are shown. The NovAtel only solution is labeled Propak_'run number' and the GPS/INS solution is labeled GPS_INS_'run number.' Table 3 includes the mean horizontal errors and the percentage of errors less than 1.5 and 5 meters for both the standalone NovAtel solution and the combined solution. The combined navigation solution exhibits improvement in all three categories with nearly 6 percentage points of improvement in the overall 5 meter error analysis.

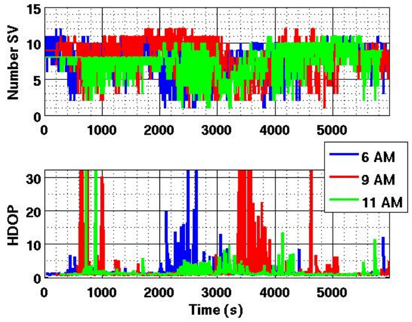

Figure 4: Number of satellites in view and HDOP for three data sets

Table 3: Error Statistics for NovAtel GPS with 6DOF IMU

Run Number	Mean Absolute Horizontal Error	% < 1.5 m	% < 5 m
Propak_R1	2.3	44.1	91.4
GPS_INS_R1	2.3	41.5	94.0
Propak_R3	2.9	46.7	88.8
GPS_INS_R3	2.0	59.8	95.5
Propak_R5	2.3	38.1	86.8
GPS_INS_R5	1.9	46.5	93.2
Propak Overall	**2.6**	**55.9**	**88.4**
GPS_INS Overall	**2.2**	**63.8**	**94.3**

Figure 5 is a zoomed view of one test run from Table 3. In Figure 5, the GPS/INS solution (green) can be seen bridging several outages of the standalone GPS solution (blue). The GPS/INS performance improvements were seen in this scenario and in heavy foliage environments.

Error statistics are shown in Table 4 as a function of the local environment. The table gives the percentage of errors less than 1.5 meters across all test runs. As seen in the table, GPS/INS integration provided the highest improvement, by percentage in the moderate and tree environments. There was also a slight improvement in the canyon areas.

Table 4: Error Statistics by Environment

Device	Environment				
	Open	Ok	Trees	Canyon	All
Propak All Runs	67	49	33	14	42
GPS_INS All Runs	74	56	40	18	49
Proportion %	4	54	15	8	100

As previously stated, the full vision system accuracy is limited by the ability to correctly identify the closest map coordinates. A map of the test route was developed using Google Earth and analysis was performed using residual errors in GPS pseudorange predictions to verify lane selection. This method did not show statistical improvement over the GPS/INS results presented earlier. One can see qualitative improvements in the positioning estimates in the downtown area in Figure 6 when using vision based estimation updates. It is anticipated that future system improvements (such as road edge detection) will provide additional information for improved identification of the lane of travel. In order to identify the potential for improvements when the correct lane is selected, the algorithm was run assuming the lane of travel was known. Modest improvement in the percentage of errors less than 1.5 meters were seen in run 1 (45.1 %) and run 3 (61.8%). It should also be noted that the accuracy of the full vision integrated system is limited by the accuracy of the map.

Figure 5: Zoom -- results of GPS/INS integration shown on satellite image of Detroit (image by *GPSVisualizer.com*)

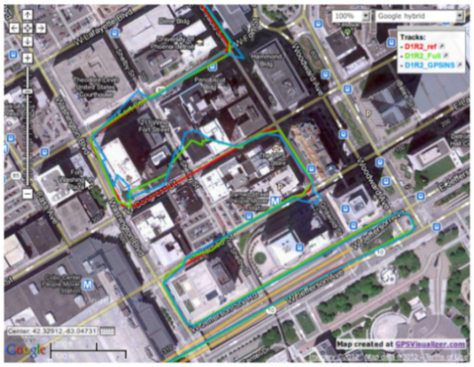

Figure 6: Results of full system with GPS/INS integration shown on a map of Detroit (image by *GPSVisualizer.com*)

V. CONCLUSIONS

In conclusion, a scalable navigation solution using typical or near typical vehicle sensors was presented. Analysis of the positioning capabilities of the system operating in various environments was shown. The GPS/INS system provided improved results over standalone GPS particularly in heavy foliage and urban canyon environments. The full system exhibited improved performance in the urban areas were GPS availability was limited. Statistical improvement using vision updates was shown for the case where the lane of travel was assumed to be known. Future work will be focused on road edge detection to provide better predictions of the lane of travel. Additionally, visual odometry will be investigated to allow vision integration when a map database is unavailable.

ACKNOWLEDGMENT

The authors would like to acknowledge the Federal Highway Administration for their support of this work. The FHWA supports several research projects critical to the transportation industry through the Exploratory Advanced Research (EAR) program. Thanks also to Jameson Colbert for his assistance.

REFERENCES

[1] P. D. Groves. *GNSS, Inertial, and Multisensor Integrated Navigation Systems*. Artech House, 2008.

[2] J. Farrel and M. Barth. *The Global Positioning System and Inertial Navigation*. McGraw Hill, 1999.

[3] U. Iqbal, A. F. Okou, and A. Noureldin, “An integrated reduced inertial sensor system—RISS/GPS for land vehicle,” in *Proc. IEEE/ION PLANS*, Monterey, CA, May 2008, pp. 912–922.

[4] North, E.; Georgy, J.; Tarbouchi, M.; Iqbal, U.; Noureldin, A.; , "Enhanced mobile robot outdoor localization using INS/GPS integration," *Computer Engineering & Systems, 2009. ICCES 2009. International Conference on* , vol., no., pp.127-132, 14-16 Dec. 2009.

[5] J. Kibbel, W. Justus, and K. Furstenberg, “Lane estimation and departure warning using multilayer laserscanner,” in *Proc. IEEE Conf. Intell. Transp. Syst.*, 2005, pp. 777–781.

[6] K. Dietmayer, N. Kapchen, K. Furstenberg, J. Kibbel, W. Justus, and R.Shulz, *Advanced Microsystems for Automotive Applications* 2005. Springer Berlin Heidelberg, 2005.

[7] A. von Reyher. A. Joos, and H. Winner, “A lidar-based approach for near range lane detection,” in *Proc. IEEE Intelligent Vehicles Symp*, 2005, pp. 147-152.

[8] C.R. Jung, C.R. Kelber, A lane departure warning system based on a linear-parabolic lane model, in: *Proc. of IEEE Intelligent Vehicles Symposium*, Parma, Italy, 2004, pp. 891–895.

[9] Y. Feng, W. Rong-ben, and Z Rong-hui, “ Based on digital image lane edge detection and tracking under structure environment for autonomous vehicle,” *Proc. IEEE Int. Automation and Logistics Conf.*, 2007, pp. 1310-1314.

[10] E. D. Dickmanns and B. D. Mysliwetz. “Recursive 3-d road and relative ego-state recognition”. 14(2):199-213, 1992.

[11] Y. Zhao, "A Map Matching Algorithm in GPS-based Car Navigation System," Intelligent Information Hiding and Multimedia Signal *Processing, 2007. IIHMSP 2007. Third International Conference* on, vol. 1, pp. 77-80, 2007.

[12] I. Miller and M. Campbell, “Particle filtering for map-aided localization in sparse gps environments,” in *Robotics and Automation, 2008. ICRA 2008. IEEE International Conference on*, 2008, pp. 1834–1841.

[13] H. Li, F. Nashashibi, and G. Toulminet, “Localization for Intelligent Vehicle by Fusing Mono-camera , Low-cost GPS and Map Data,” in *Proceedings of IEEE Annual Conference on Intelligent Transportation Systems*, 2010, pp. 1657–1662.

[14] D. Bevly, and S. Cobb. *GNSS for Vehicle Control*. Artech House, Boston, 2010.

[15] J.-H. Wang and Y. Gao, “The aiding of MEMS INS/GPS integration using artificial intelligence for land vehicle navigation,” *IAENG Int. J. Comput. Science*, vol. 33, no. 1, pp. 33-1–33-11, 2007

[16] J. Britt, “Lane tracking using multilayer laser sacnner to enhance vehicle navigation and safety,” *Proc. 2009 International Techincal Meeting of Institute of Navigation*, Anaheim, 2009.

[17] C. Rose, “Vehicle lane position estimation with camera vision using bounded polynomial interpolated lines,” *Proc. 2009 International Technical Meeting of Institute of Navigation*, Anaheim, 2009.Hegarty, C. and Kaplan, E. D., (editors) “Understanding GPS: Principles and Applications, 2nd ed.,” Artech House, Norwood, MA, 2006.

[18] Hegarty, C. and Kaplan, E. D., (editors) “Understanding GPS: Principles and Applications, 2nd ed.,” Artech House, Norwood, MA, 2006.

[19] U.S. Department of Transportation, Federal Highway Administration, “Annual Vehicle-Miles of Travel 1980-2007, By Functional System, National Summary (Table VM-202, summary for 2007),” Jan. 2009, http://www.fhwa.dot.gov/policyinformation/statistics/vm02_summary.cfm.

[20] P. Newman, “MOOS – A Mission Oriented Operating Suite,” MIT Department of Ocean Engineering, Tech. Rep. OE-2003-07,2003.

[21] Parkinson B.W. and Spilker J.J. *The Global Positioning System: Theory and Applications Volume I*. Aiaa, 1996.